ChemPhysChem

Research Article
doi.org/10.1002/cphc.202400486

Chemistry Europe
European Chemical Societies Publishing

www.chemphyschem.org

Surface Gold Atoms Determine Peroxidase Mimic Activity in Gold Alloy Nanoparticles

Giulia Maria Spataro,[a] Jijin Yang,[a] Vito Coviello,[a] Stefano Agnoli,[a] and Vincenzo Amendola*[a]

The development of peroxidase mimic nanocatalysts is relevant for oxidation reactions in biosensing, environmental monitoring and green chemical processes. Several nanomaterials have been proposed as peroxidase mimic, the majority of which consists of noble metals and oxide nanoparticles (NPs). Yet, there is still limited information about how the change in the composition influences their catalytic activity. Here, the peroxidase mimic behaviour of gold NPs is compared to a traditional nanoalloy as Au–Ag and to the Au–Fe and the Au–Co nanoalloys, which were not tested before as oxidation catalysts. Since the alloys of gold with iron and cobalt are thermodynamically unstable, laser ablation in liquid (LAL) is exploited for the synthesis of these NPs. Using LAL, no chemical stabilizers or capping agents are present on the NPs surface, allowing the evaluation of the oxidation behaviour as a function of the alloy composition. The results point to the importance of surface gold atoms in the catalytic process, but also indicate the possibility of obtaining active nanocatalysts with a lower content of Au by alloying it with iron, which is earth-abundant, non-toxic and low cost. Overall, Au nanoalloys are worth consideration as a more sustainable alternative to pure Au nanocatalysts for oxidation reactions.

Introduction

Catalysts of biological oxidation reactions are interesting for a wide range of applications, such as immunoassays, biochemical production of feedstocks, environmental monitoring and remediation.[1–3] In these reactions, hydrogen peroxide or organic hydroperoxides are reduced by interacting with a suitable substrate that acts as an electron donor.[4] Natural enzymes such as horseradish peroxidase (HRP) and glucose oxidase have been widely exploited to catalyse biological oxidation reactions due to their high efficiency and specificity.[5] However, natural enzymes can suffer from some inherent disadvantages, such as high cost, instability during storage and at high temperatures, strong dependence of catalytic activity on the reaction environment, and possible inhibition by the presence of heavy metal ions and other substances such as thiols and azides.[3,6–9]

In recent decades, numerous attempts have been made to produce artificial enzymes as more stable and cost-effective alternatives to natural enzymes, including porphyrins, supramolecular constructs, bioorganic compounds and metal complexes.[10] After the early 2000s,[11] nanomaterials and nanoparticles (NPs) have been also studied as possible alternatives to natural enzymes because of their large surface-to-volume ratio.[12] For several of these nanosystems, the kinetic behaviour of enzymes was observed, thus they were termed "nanozymes" to identify the class of artificial nanostructures with an intrinsic catalytic activity mimicking natural enzymes.[11,12] The first example of "nanozyme" was based on suitably functionalized gold NPs,[11] which showed exceptional properties for the improvement of colorimetric assays, enabling the development of innovative diagnostic tests.[13] Only in 2007, however, it was found that NPs of Fe_3O_4 possessed intrinsic enzyme mimic activity similar to that found in natural peroxidases, and were able to catalyse the oxidation of 3,3′,5,5′-tetramethylbenzidine (TMB) in the presence of hydrogen peroxide.[14] Subsequently, peroxidase- or oxidase-like activities were found in several other nanomaterials, such as positively charged Au NPs.[15] This prompted the research on various gold-based nanosystems as peroxidase mimics, focusing on the structural and chemical aspects which influence their activity.[16–20] However, despite the intense research aimed at exploring the catalytic activity in Au NPs of different shapes and sizes,[18–21] little is known regarding the role of surface gold atoms in nanoalloys-based peroxidase analogues. Nanoalloys are promising candidates as enzyme mimics due to the possibility of modulating their properties and stability by controlling the composition and structure.[17,22–25] Gold-based nanoalloys often show remarkable performance compared to their monometallic counterparts and have attracted increasing interest from the scientific community.[23,26] For instance, Au–Ag bimetallic nanostructures exhibited stable peroxidase catalytic activity at acidic pH, which can be controlled by alloy composition and solution pH.[27,28] Better peroxidase-like performances than the monometallic counterparts have been observed also in bimetallic gold heterostructures due to synergistic effects between the constituent elements.[29] Another potential advantage of gold-based nanoalloys is the use of transition metals and rare earths, which reduces the use of expensive metals typically used in conventional catalysis, such as silver, platinum and palladium.[30,31] An

[a] G. M. Spataro, J. Yang, V. Coviello, S. Agnoli, V. Amendola
Department of Chemical Sciences, University of Padova, Padova, Italy
E-mail: vincenzo.amendola@unipd.it

example is the Au–Fe nanoalloy, which combines the properties of gold, such as surface plasmon resonance, with the magnetic behaviour of iron, and has applications in magneto-optics and catalysis.[32,33] On the other hand, the catalytic mechanism of nanoalloys differs with composition and stoichiometry depending on the different valence electron configurations and the type of enzymatic activity they exhibit.[17,23] These considerations justify the interest in the production of multielement gold-based nanocatalysts to investigate their peroxidase-like catalytic properties.

However, the preparation of nanoalloys using conventional physical or chemical techniques is not always straightforward, for example due to the immiscibility of metallic elements or the large difference in their redox potentials.[22,24] The laser-assisted synthesis in liquid, which operates under conditions far from equilibrium, can overcome these difficulties by enabling the production of metastable phases, such as immiscible metal element nanoalloys.[22,24,34,35] In particular, laser ablation in liquid (LAL) is a promising technique for fine-tuning the surface, electronic and crystalline structure of nanomaterials, with several advantages over conventional chemical and physical synthesis routes.[22,24,31,34,36] LAL is a green procedure for obtaining colloidal suspensions in water or organic solvents, without the use of surfactants or capping agents.[22,37–39] This allows obtaining NPs with free surfaces, which is crucial for catalytic applications, not to mention that NPs purification procedures often require time-consuming and costly steps.[22,24,31,34,37,38] In this regard, it has been shown that catalytic NPs produced by LAL achieved five times more surface coverage than their counterparts obtained through the chemical route, leading to better efficiency in surface interaction with adsorbates.[40,41]

Of the various nanoalloys produced by LAL, Au–Ag is one of the best-known examples, thanks to the ease of synthesis resulting from the miscibility of Ag and Au throughout the compositional range of the alloy; a feature that allows the production of these nanoalloys also by other synthetic routes, such as chemical reduction.[42] However, the formation of nanoalloys with elements other than Au and Ag by conventional synthetic routes is often very challenging.[24] For example, it is impossible to form Au–Fe and Au–Co nanoalloys under normal environmental conditions due to their wide immiscibility range and ease of oxidation of the transition metals.[33,43] Syntheses using precursors in solution generally occur close to the thermodynamic equilibrium, which for these two elements would result in hybrid structures of segregated phases rather than a nanoalloy. Conversely, the LAL of bulk Au–Fe and Au-Co targets in ethanol produced, respectively, Au–Fe and Au–Co nanoalloys that were investigated for magnetic and plasmonic applications.[33,43]

Here, LAL was exploited to produce uncapped nanoalloys of Au–Ag, Au–Fe and Au–Co to study the effect of the composition on the peroxidase mimic activity in comparison to pure LAL-synthesized Au NPs obtained by the same technique. The results contribute to elucidating the role of the chemical elements in the nanocatalysts for oxidation reactions of great applicative interest in multiple fields related to the detection and conversion of chemical species.

Experimental

Synthesis. LAL started from bulk targets (Au, Au/Ag 90/10 weight % (wt%), Au/Fe 90/10 wt%, Au/Co 90/10 wt%, purity >99.9%, from Mateck) in batches of 130 mL of ethanol (HPLC grade, >99.9%, Sigma-Aldrich), kept under argon flux and continuous magnetic stirring. Laser pulses at 1064 nm, repetition rate 50 Hz, duration of 6 ns, were focused with an f 100 mm lens up to a fluence of 14 J/cm^2 and for an ablation time of 150 min for each batch. To ablate the whole target surface, the cell was mounted on a motorized XY scanning stage (Standa) managed with a 2-axis stepper and a DC motor controller.

The number of synthesis batches was 2 for Au and 3 for Au/Ag, Au/Fe and Au/Co targets. All the batches from the same target were grouped just after reducing the synthesis volume from the initial 130 mL to approximately 20 mL using a rotary evaporator at 30 °C. Then, a solution of disodium ethylenediaminetetraacetic acid (EDTA, Sigma-Aldrich, 3 mg/mL) in distilled water was added in a 1:1 volume ratio to all the colloids and the mixtures heated in a thermal bath at 60 °C for 1 h. Subsequently, the solutions were centrifuged at 1000 rcf for 30 min with a fixed angle rotor to remove the supernatant, and the nanoparticles were redispersed in 30 mL of distilled water. The solutions were then washed 3 times at 4000 rcf for 1 h with distilled water and finally redispersed in 3 mL of HPLC grade ethanol. The final concentration of each sample was determined by Inductively Coupled Plasma-Mass Spectrometry (ICP-MS) analysis.

Characterization. UV-visible absorption spectroscopy was performed with a JASCO V770 UV-vis-NIR spectrometer in 2 mm quartz cells. Transmission electron microscopy (TEM) analysis was performed with an FEI Tecnai G2 12 operating at 100 kV and equipped with a TVIPS CCD camera.

Scanning TEM (STEM), energy dispersive X-ray (EDX) spectroscopy and high resolution (HR) TEM analysis were performed with a JEOL JEM–F200 TEM operating at 200 kV, equipped with a cold FEG gun and a windowless silicon drift EDX detector.

The samples for TEM analysis were prepared by evaporating a few μL of a highly diluted NP suspension on a copper grid coated with a carbon film. Size histograms were obtained with ImageJ using a minimum of 500 NPs for each sample. ICP-MS measurements were performed with an ICP-MS Agilent 7700x (Agilent Technologies, equipped with an octupole collision cell operating in kinetic energy discrimination mode). Powder x-ray diffraction (XRD) analysis was performed with a Panalytical XPert 3 Powder diffractometer equipped with a Cu tube (40 kV, 40 mA), a BBHD mirror, a spinner and a PIXcel detector. The samples were deposited on Si zero-background substrates by drop casting and drying at room temperature. Crystalline phase identification and Rietveld analysis were executed with the Crystallography Open Database (COD) implemented in the EVA and TOPAS V6 software. Energy dispersive X-ray (EDX) spectroscopy measurements coupled with scanning electron microscopy (SEM) were performed with an environmental SEM model FEI Quanta 200. The samples were obtained by dropwise deposition of NPs dispersion on a glassy carbon sample holder and drying at room temperature.

The X-ray photoelectron spectroscopy (XPS) analysis was performed at room temperature in an ultra-high vacuum system at a pressure below 10^{-9} mbar using normal emission geometry with a modified VG ESCALAB MKII (Vacuum generators, Hastings, England)

equipped with a twin (Mg/Al) anode X-ray source, an Ar^+ ion sputter gun (VG EX05), and a hemispherical electrostatic analyzer with a five-channels detector. As an excitation source, we used Al–Kα radiation (1486.6 eV). For sample preparation, an appropriate volume of nanoparticles in ethanol (approximately 50 μL) was deposited by drop casting onto a glassy carbon substrate that had previously been cleaned with a diamond paste of different grain sizes and repeated washing with isopropanol followed by sonication. The samples were degassed for several hours before analysis.

Ar^+ sputtering was performed at 1.5 keV in normal incidence for 30′ minutes with the ion gun working at 5 10^{-6} mbar background pressure. The sputtering rate in these conditions was determined by comparison with Fe_3O_4 thin films grown on Au(111) single crystal, where the Fe 2p vs Au 4f signal ratio was monitored as a function of sputtering time (total sputtering current on a gold sample with 2 cm^2 area is 4–6 μA). Under these conditions, the sputtering rate of the oxide layer resulted in 1 ± 0.5 nm in 30′.

Catalytic tests. For the peroxidase-mimic catalytic tests, a standard procedure was used,[44,45] based on the oxidation of TMB (Sigma-Aldrich, >99%) by hydrogen peroxide (H_2O_2, 30 wt% in H_2O, Sigma-Aldrich). In this procedure, 20 μL of a 150 mM TMB stock solution in DMSO (HPLC grade, Sigma-Aldrich), 375 μg of Au (for Au NPs and Au nanoalloys) or Fe (for Fe_3O_4 NPs, Sigma Aldrich, <5 microns, 98%) from the stock NPs solutions in ethanol and, finally, 83 μL of 30 wt% H_2O_2 were sequentially added to 15 mL of distilled water buffered solution contained in a 40 mL cylindrical glass vial. The resulting final concentrations were 200 μM for TMB, 25 μg/mL for the reference metal (Au or Fe), and 70 mM for H_2O_2. The Au NPs and Fe_3O_4 NPs were mixed in the same Au:Fe molar proportions measured for the Au–Fe NPs. The mixture was performed before the catalytic tests and with the same acidic buffer, collecting the particles by centrifugation at a low centrifugal speed of 150 rcf to guarantee the formation of an Au-Fe_3O_4 nanocomposite.

The pH of the aqueous solution was controlled using a sodium acetate/acetic acid (NaAc/HAc) buffer prepared in distilled water with HAc (Sigma-Aldrich) and NaOH (Sigma-Aldrich) in appropriate proportions. The measurements were carried out following the evolution of the optical absorption spectra of the solution *in situ* and in real-time using a peek-coated fiber-optic probe connected to a portable UV-vis spectrophotometer (StarLine AvaSpec-ULS-EVO). The spectra were acquired every 30 s and for a total acquisition time of 20 minutes. The reaction vial, into which the spectrophotometer probe was inserted, was kept under stirring and placed in a water bath to maintain a constant temperature of 40 °C during the reaction. Each TMB solution in NaAc/HAc buffer was degassed by vacuum pumping before the addition of NPs and hydrogen peroxide to avoid the drawback associated with the formation of gas bubbles on the surface of the spectrophotometric probe, provoking light scattering of the radiation and making the measurements poorly reproducible. The catalytic activity was obtained by calculating the slope of the absolute change of absorbance at 652 nm versus time.

Results

Synthesis and Characterization of Nanocatalysts

In order to have homogeneous synthetic conditions, the gold and alloy NPs were all generated by LAL in pure ethanol under Ar flux, collected by centrifugation after incubation with EDTA for 1 h at 60 °C and, finally, resuspended in pure ethanol (Figure 1A). The optical features typical of the different metal NPs are identified with UV-vis spectroscopy (Figure 1B). Since the NPs are collected in pure ethanol without any capping agent or other chemical additive, only the interband transitions of gold, silver and their alloys are found in the UV range,[24,33,43] which is free of absorption bands from other chemicals. In the visible range, alloying leads to a reduction in the intensity of the localized surface plasmon (LSP) absorption in Au–Fe and Au–Co nanoalloys compared to pure Au NPs. It has been previously shown that Au NPs surrounded by iron oxide NPs or by a continuous shell still retain an intense plasmonic response and undergo the red shift of the LSP,[33,46] which is not the case for the Au–Fe and Au–Co nanoalloys samples. In these samples, the attenuation is due to the changes in the band structure of gold upon alloying with the two transition metals.[24,43] Fe and Co atoms have partially occupied *d*-levels, which are also present around the Fermi energy in alloys with plasmonic metals. These electronic levels, known as virtual bonded states (VBS), cause the damping of the LSP peak due to the introduction of low-frequency inter-band transitions (LFIB),

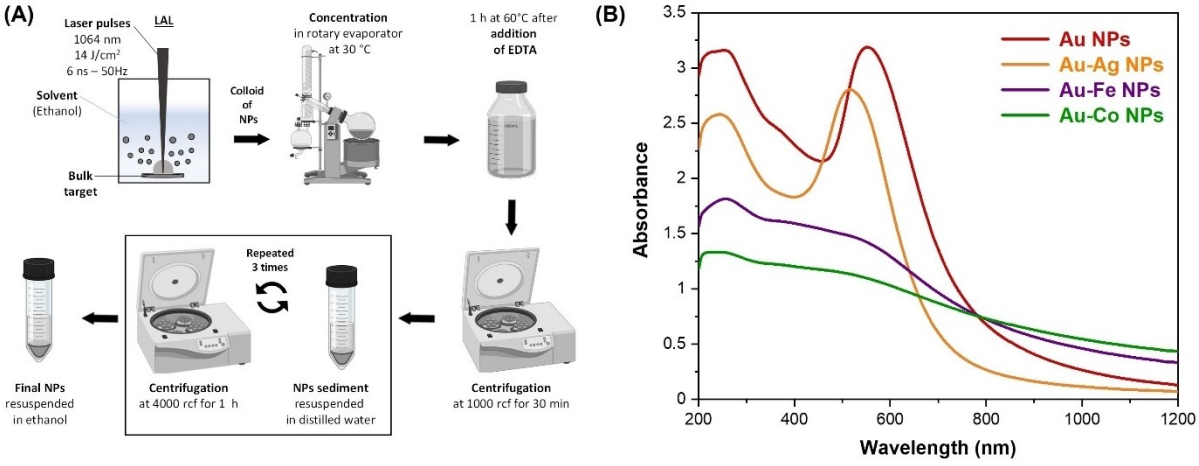

Figure 1. (A) Schematic depiction of the NPs synthesis. Created with BioRender.com. (B) UV-vis absorption spectra of the four samples dispersed in ethanol.

which constitute a significant source of coherence loss and electrostatic screening in the collective excitation of free electrons.[33,43] The same cannot be said for the nanoalloy of the two renowned plasmonic metals Au and Ag, which have LSP intensity and width comparable to those of pure gold NPs, although with a blue shift toward the spectral range of spherical Ag NPs in reason of the bimetallic nature. In fact, the formation of Au–Ag nanoalloys has been widely exploited for the nearly linear tuning of the LSP band position by continuously controlling the Au/Ag ratio over the entire compositional range of the alloy.[47] The SPR maxima of Au–Fe and Au–Co NPs, although barely identifiable, also are blue-shifted compared to Au NPs. However, the blue shift of the Au–Ag NPs is due to the location in the UV of the interband transition of pure silver, which allows the existence of an LSP band at shorter wavelengths. A different argument must be made for systems containing Fe and Co, where the blue shift in the LSPR is due to the increase in the electronic density of the alloys compared to pure Au. This is the effect of both the higher number of conduction electrons and the lattice contraction in these nanoalloys, and contributes further to the LSP damping due to the increased overlap with the interband transitions inherent in the gold electronic structure.[33,43]

From a more specific examination of the position of the LSP bands, one can observe that the maxima are at 552 nm for Au NPs, 517 nm for Au–Ag NPs, and in the 540–545 nm range for the Au–Fe and Au–Co NPs. These spectral positions are red-shifted compared to what is typically expected for isolated spherical NPs, indicating that the particles are agglomerated during the synthetic procedure, due to the absence of surface stabilizers and the centrifugation and redispersion cycles. Nonetheless, all samples were stable and easily dispersible in ethanol, as required for characterization and exploitation in the catalytic tests.

The TEM images (Figure 2) corroborate the evidence of particle agglomeration because all four samples are constituted by NPs with a spherical morphology and always clustered together on the carbon film of the TEM grid. The size histograms indicate that the NPs all have a size distribution in the interval between a few nm and tens of nm, as it is typical for metal particles produced by LAL with ns pulses.[22,31,40,48] The average size measured from the TEM analysis is 8 ± 4 nm for Au NPs, 15 ± 6 nm for Au–Ag NPs, 18 ± 10 nm for Au–Fe NPs, and 13 ± 7 nm for Au–Co NPs.

Further information on the size of crystalline domains and the phase of the NPs was achieved by powder XRD analysis (Figure 3A). The XRD patterns show that all the samples have the face-centered cubic (FCC) lattice typical of pure gold, without any other contribution. Besides, from the comparison of the diffraction patterns, it is possible to observe the difference in the position of the reflections of the Au–Fe and Au–Co samples compared to those of the pure gold and Au–Ag samples. In fact, while Au and Ag have similar lattice parameters and their alloying cannot be accurately discriminated from a standard XRD analysis, Au–Fe and Au–Co nanoalloys undergo a contraction of the FCC lattice parameter when the transition metals are included in the cubic cell as random substitutional impurities.[49] Hence, the lattice parameter of each phase was extracted from the Rietveld refinement of the XRD pattern, and the average crystallite size was calculated from Scherrer's equation on the most intense peak. The cell parameter resulted in 4.075 Å for Au NPs (literature 4.079 Å), 4.070 Å for Au–Ag NPs, 4.020 Å for Au–Fe NPs, and 4.009 Å for Au–Co NPs, confirming the lattice contraction in the Fe and Co nanoalloys compared to pure gold. Using Vegard's law, the composition of the Fe and Co nanoalloys was calculated as, respectively, 17 ± 1 atomic % (at%) of Fe and 18 ± 1 at% of Co. The calculation is based on the previously verified hypothesis that, for the Au–Fe and Au–Co alloys with a prevalence of gold, the atomic volume of the alloy is a continuous function of the composition.[49,50]

The average crystallite size resulted in 13 nm for Au NPs, 12 nm for Au–Ag NPs, 15 nm for Au–Fe NPs, and 21 nm for Au–Co NPs. The trend confirms that the Fe and Co nanoalloys have larger sizes than Au and Au–Ag samples, previously evidenced by the average geometrical size measured from TEM images. However, the quantities accessible with the two techniques differ because the XRD data are volume-weighted and, in any case, refer to crystalline domains, while LAL is well known to produce polycrystalline particles.

The elemental composition of the four samples was confirmed further with the SEM-EDX analysis. For the Au, Au–Ag, Au–Fe and Au–Co samples, the characteristic X-ray emission spectra only show the peaks of gold and of the alloying elements, where present, superimposed to the peaks originated by the glassy carbon substrate (Figure 3B). The EDX analysis estimated a silver content of 23 ± 3 at% for the Au–Ag NPs, an iron content of 17 ± 3 at% for the Au–Fe NPs, and a cobalt content of 19 ± 4 at% for the Au–Co NPs. ICP-MS was used to complete the assessment of nanoalloy composition and quantify the concentration of the samples, resulting in a silver content of 25 ± 3 at% for the Au–Ag NPs, an iron content of 23 ± 3 at% for the Au–Fe NPs, and a cobalt content of 19 ± 3 at % for the Au–Co NPs. Overall, all the elemental compositions obtained by the Vegard law, the EDX spectroscopy and the ICP-MS analysis are comparable to each other considering the uncertainty inherent to each technique (Figure 3C).

The surface composition of the nanoalloys may differ significantly from the average composition, especially in this case where the elements in the alloy also differ in oxidation potentials and surface energy. Therefore, the XPS analysis was performed on the Au–Ag, Au–Fe and Au–Co nanoalloys to assess the chemical nature and the stoichiometry at the surface of the NPs. Besides, this information was distinguished for the topmost and the underlying atomic layers by collecting the photoelectron emission spectra before and after sputtering with Ar^+ ions. The gold signals are consistent in all samples (Figure 4) and show a single Au $4d_{5/2}$ peak at 335 eV, the expected energy for metallic gold, both before and after sputtering. From the XPS analysis obtained for the Au–Ag sample (Figure 4A and B), it can be seen that the position of the Ag 3*d* peaks remains unchanged even after sputtering, although its intensity decreases corresponding to a change in the composition, which goes from the 51 ± 5 at% of Au and 49 ± 5 at% of Ag before sputtering, to the 75 ± 5 at% of Au and

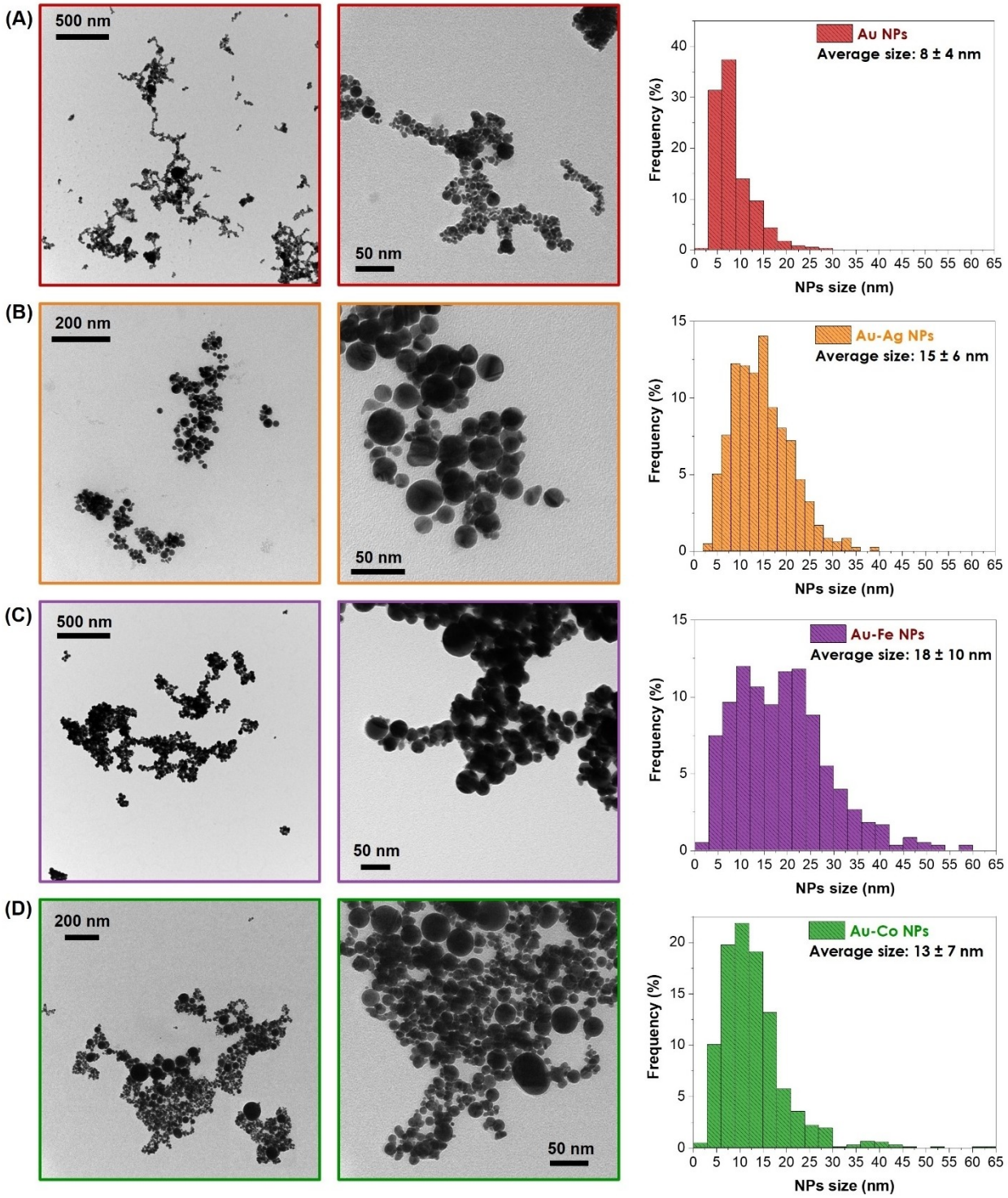

Figure 2. Representative TEM images (left) and size histograms (right) of the Au (A), Au–Ag (B), Au–Fe (C) and Au–Co (D) NPs.

the 25 ± 5 at% of Ag after sputtering. This leads to the conclusion that there is a depletion of gold content in the topmost layers of the Au–Ag nanoalloy compared to the innermost layers. The energy values of the 3*d* photoemission lines (Figure 4B) and the Auger M_5VV signal of silver (Figure 4C) fall within the region of the silver alloys.[51–53] Besides, after sputtering we observe a kinetic energy shift of the Auger M_5VV signal of silver (+0.3 eV) in concomitance with the decrease of its elemental abundance, as expected for an alloy with noble metals.[51–53]

The XPS surveys obtained for the Au–Fe sample (Figure 4D) show a change in the atomic iron content from 8 ± 5 at% before sputtering to 18 ± 5 at% in the innermost layers. In addition, the multipeak analysis with Gupta-Sen multiplets[54] of the Fe $2p_{3/2}$

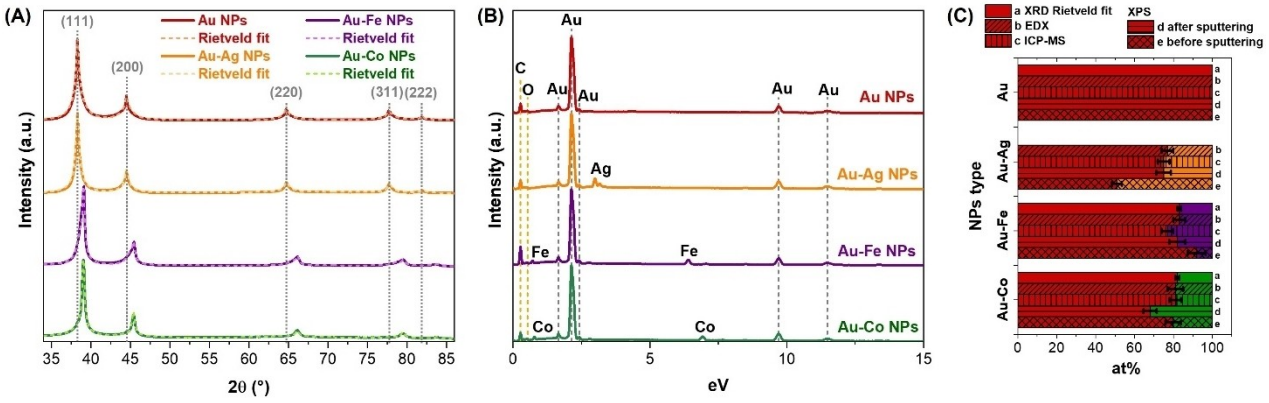

Figure 3. (A) XRD analysis and Rietveld refinement of the four samples. The diffractograms were normalized to the most intense reflection of the FCC pattern and vertically shifted for a clearer comparison. (B) SEM-EDX elemental analysis for the identification of the nanoalloy composition. The spectra were normalized to the most intense peak of the Au component and vertically shifted for a clearer comparison. (C) Summary of the atomic composition of the four samples obtained with the different characterization techniques.

peak (Figure 4E) indicates that the surface of the nanoalloy is richer in oxidised FeO than in metallic Fe, with a relative Fe(II): Fe(0) abundance of 69:31 before sputtering, decreasing to 59:41 after sputtering.

Similar to the Au–Fe sample, also the XPS surveys of the Au–Co sample (Figure 4F) show the increase in the atomic content of Co from 20 ± 5 at% before sputtering to 32 ± 5 at% after it, as well as the predominance of oxidised Co at the surface before sputtering (70%), which decays to only 19% after sputtering according to the fitting[55] of the Co $2p_{3/2}$ peak (Figure 4G). This change is accompanied by the variation in the oxidation state of the oxidised Co component, which belongs to Co_3O_4 before sputtering and to CoO after sputtering.

The experimental evidence that Fe and Co are more oxidised on the surface of the nanoparticles than in the inner layers, as well as the higher abundance of gold in the topmost layers of the Au–Fe and Au–Co nanoalloys, both agree with the literature and with the chemical treatment executed on the NPs with EDTA to clean the surface of the nanoalloys from non-crystalline components which appear during the LAL.[49,50,56] The tendency of the transition metals to oxidise readily in the presence of trace oxygen molecules and the miscibility gap with gold ineluctably introduced a little extent of dealloying during the whole synthetic procedure. This phenomenon is not avoided even if ethanol molecules are pyrolyzed into reducing compounds which exert a protective effect against oxidation during metal ablation and NPs formation.[49,50,56]

A further assessment of the nanoalloys structure was undertaken with STEM and HRTEM imaging and STEM-EDX analysis (Figure 5). The high-angle annular dark field (HAADF) STEM did not evidence core-shell or heterogeneous domains in the three types of alloy NPs. HRTEM images evidenced that the NPs are polycrystalline and rich in defects, but no core-shell or heterostructures are found. The EDX bidimensional maps and linescans further confirmed the homogeneous distribution of the alloying elements in the three samples. Overall, the DF-STEM, STEM-EDX and HRTEM analyses agree with the XRD and UV-vis absorption results, since none of them has evidenced the presence of crystalline iron or cobalt oxide in the samples. Besides, crystalline oxide signatures were not found in the XRD patterns of the nanoalloys obtained just after the LAL synthesis and before the cleaning procedure with EDTA. As described previously about the LAL in ethanol of the same bimetallic targets,[49,50] iron and cobalt are released as poorly crystalline or amorphous compounds which are etched by the chelating agent.

Therefore, the characterization of the NPs demonstrated that the non-equilibrium synthetic conditions typical of LAL were such to overcome the thermodynamic limits to the miscibility of gold with iron or cobalt, making these nanoalloys available for the investigation of their peroxidase mimic activity in comparison with Au and Au–Ag NPs.

Catalytic Tests

The oxidation of TMB by hydrogen peroxide can be used to quantitatively analyse the peroxidase activity of nanocatalysts by spectroscopically monitoring the transformation of TMB over time.[44,57] After oxidation of the diamine with H_2O_2, the resulting diimine forms a charge transfer complex with another TMB molecule.[44,57] Contrary to TMB, which has an absorption maximum at 285 nm, the complex has two absorption peaks falling at 370 nm and 652 nm and is in rapid equilibrium with the radical cation form of the TMB. However, the equilibrium is strongly shifted towards the complex, whose further oxidation leads to the formation of a diimine stable at acidic pH and with an absorption band at 450 nm.[44] Figure 6A shows the time course of the UV-vis spectra recorded during the oxidation of TMB by H_2O_2 catalysed by Au NPs at pH 3.8. The increase in intensity of the absorption peaks at 370 nm and 652 nm corresponds to the increase in concentration of the charge-transfer complex over time. The start of the oxidation of the complex leading to the formation of the isolated diimine, instead, appears at much longer times as the increase in the intensity of the peak at 450 nm. This is evidenced by the colour

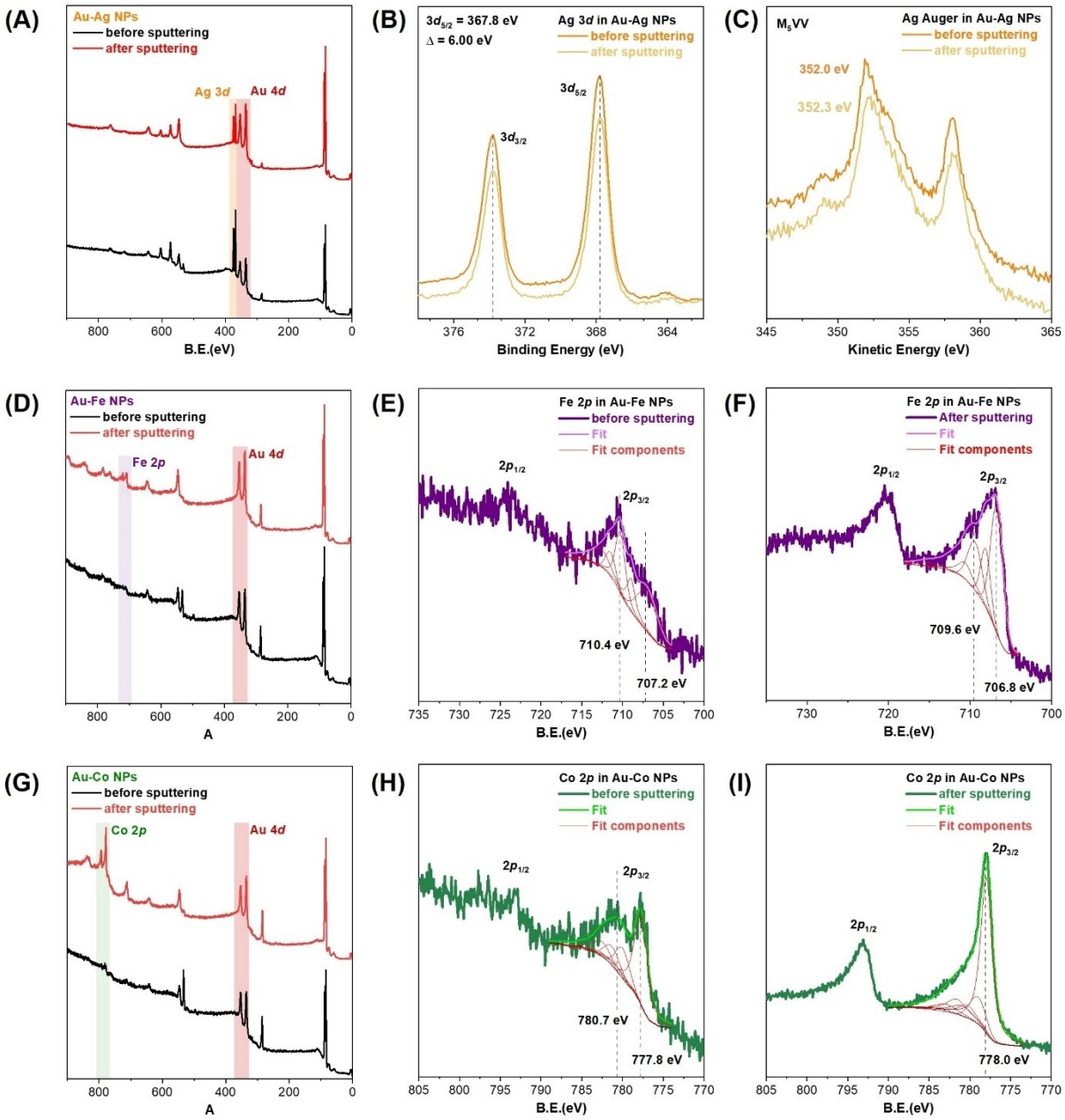

Figure 4. XPS analysis of the four samples. (A) Survey before and after Ar^+ ion sputtering on the Au–Ag sample. (B) Au 3*d* peak before and after sputtering. (C) Au Auger $M_{4,5}VV$ line before and after sputtering. (D) Survey before and after Ar^+ ion sputtering on the Au–Fe sample. The Fe 2*p* peaks before (E) and after sputtering (F) are also reported with the relative fitting of the $2p_{3/2}$ component. (G) Survey before and after Ar^+ ion sputtering on the Au–Co sample. The Co 2*p* peaks before (H) and after sputtering (I) are also reported with the relative fitting of the $2p_{3/2}$ component.

change of the reaction solution, which first turns from colourless to blue, at longer times (>20′ in our conditions), passes through a green stage, and finally turns yellow, with the green solution due to the mixture of the blue complex and the yellow isolated diimine.

For the quantification of the catalytic activity of the NPs, only the time-dependent absorption peak at 652 nm is considered (Figure 6B), because the absorption at 370 nm may partially overlap with the free diimine peak at 450 nm.[44] In the initial phase of the reaction, there is a linear trend of the absorbance as a function of time, which then slows down to a plateau in a subsequent phase of the reaction, where the concentration of the charge transfer complex reaches a saturation level. This point marks the beginning of TMB conversion into the fully oxidised product. The linear increase in absorbance as a function of time in the initial phase of the catalytic reaction allowed the description of the experimental data according to first-order kinetics.[44,57]

However, natural and artificial oxidation catalytic systems are sensitive to the pH of the reaction environment.[44,57,58] The pH-dependent reactivity results also from the limited solubility of TMB in aqueous solutions, which is improved at acidic pH by

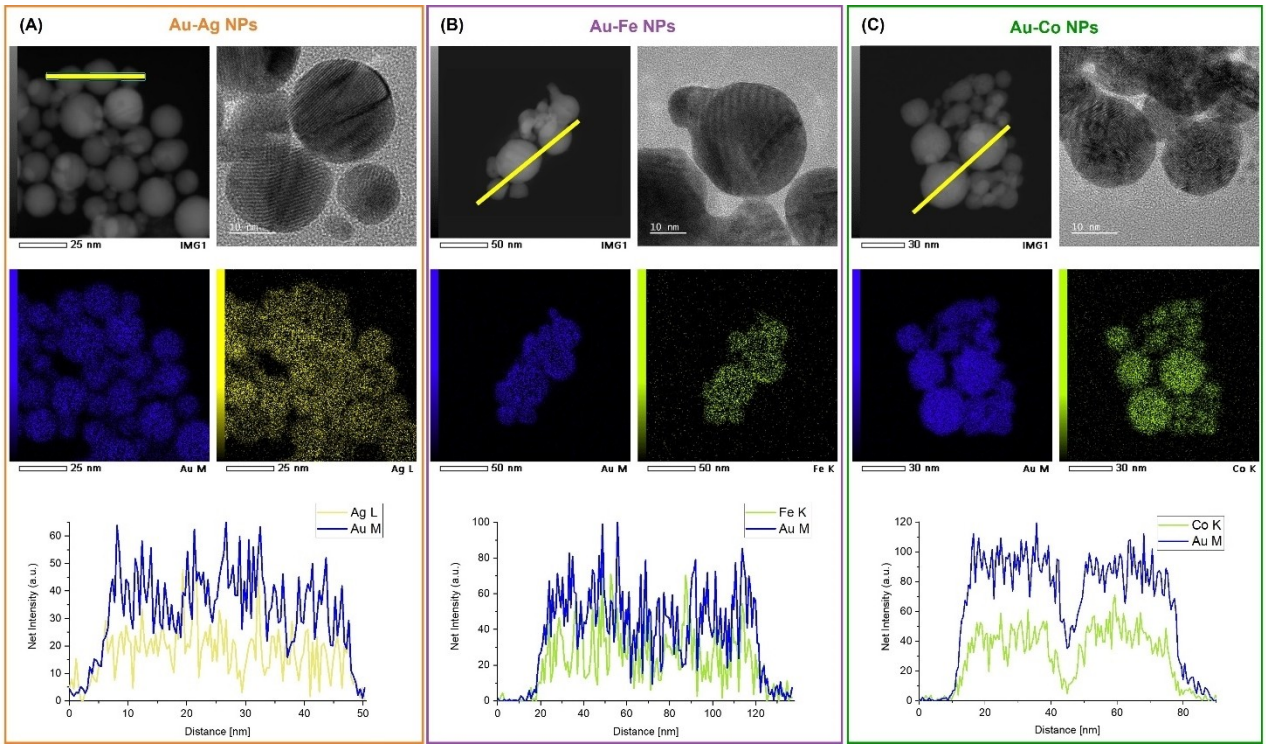

Figure 5. HAADF-STEM, HRTEM, STEM-EDX net intensity maps and linescans of the Au–Ag (A), Au–Fe (B) and Au–Co (C) nanoalloys. Au M-line, Ag L-line, Fe K-line and Co K-line were used for the EDX maps. The linescan for each sample was collected along the yellow line in the corresponding STEM-DF image.

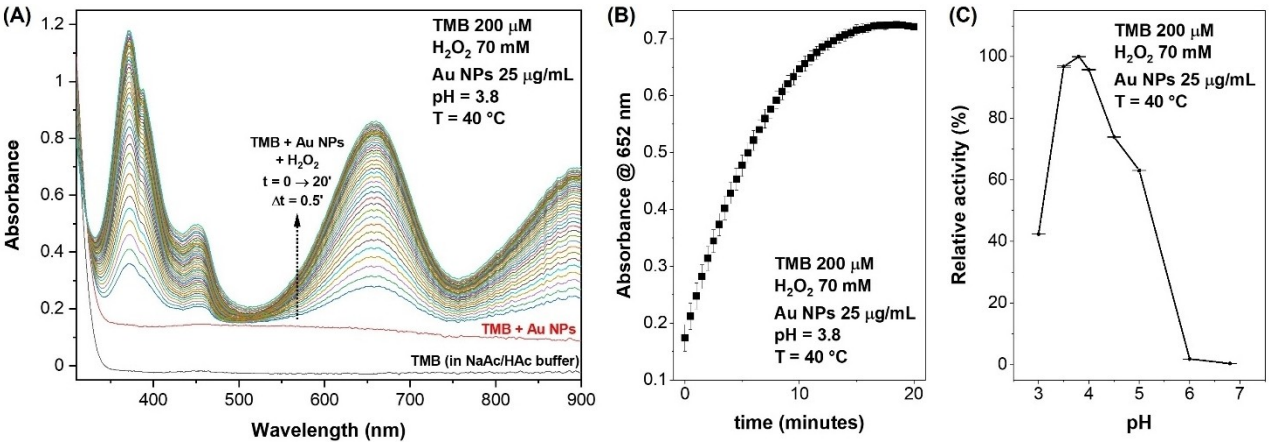

Figure 6. (A) time evolution of TMB spectra at pH 3.8 obtained from experiments performed under standard reaction conditions reported in the graph using Au NPs as the catalyst. (B) Time evolution of the absorbance peak at 652 nm obtained for the experiment reported in (A). (C) Relative catalytic activity as a function of pH in the standard reaction conditions reported. Error bars in (B) and (C) are the semidispersion over two replicated experiments.

protonation of one of the amine groups of the substrate. However, excessive lowering of the pH causes protonation of both amine groups and renders the substrate insensitive to catalytic oxidation.[58] Furthermore, the formation of the blue-coloured charge transfer complex requires the presence of unoxidized TMB in equilibrium with the cationic radical.[58]

Therefore, Au NPs were used as a reference to find the optimal pH conditions under which studying the catalytic process also on the nanoalloys, and the other reaction parameters were taken like those typically found in the literature, corresponding to a temperature of 40 °C, a concentration of TMB in the order of 10^{-6} M and a concentration of H_2O_2 of the order of $10^{<->3}$ M, i.e. in large excess over the substrate.[14,57,59,60] Figure 6C shows the relative activity (in % referred to as the highest activity) for Au NPs at pH values ranging from 3 to 6.8. The maximum is obtained at pH 3.8, which is chosen as the optimal value for the following catalytic tests. This is in agreement with the best pH operating values typically reported for Au and Fe_3O_4 NPs, as well as for HRP, in similar conditions of temperature and concentration of TMB and H_2O_2, which are defined by the pH-dependent solubility of TMB.[14,16–20]

The absorbance increase at 652 nm, measured on the nanoalloys during the catalytic experiments, is summarised in Figure 7A and compared to that of pure Au and of the solution without NPs (TMB + H_2O_2). The time interval is limited to the first 10 minutes of the reaction to give a clearer presentation of the experimental data, while Figure 7B is a magnification of the linear range, from which initial velocity values are determined. The histogram of initial velocities with the corresponding uncertainty is shown in Figure 7C. It is easily appreciated that Au NPs have higher initial velocity as well as overall conversion ability than the nanoalloys, although the Au–Fe NPs are only slightly less active, whereas the Au–Co and Au–Ag nanoalloys performed significantly worse. Nonetheless, the uncatalyzed reaction between TMB and H_2O_2 has the lowest initial velocity and overall conversion, confirming the catalytic efficacy of all the NPs tested. To clarify the role of iron in combination with gold, the experiments were performed also with commercial Fe_3O_4 particles (at a final concentration of 25 μg Fe/mL), and a mixture of Au NPs (at the same concentration of the other tests, 25 μg Au/mL) and Fe_3O_4 particles (at an iron concentration equivalent to that of Fe in the Au–Fe NPs according to the structural characterization). While the Fe_3O_4 particles alone have the lowest activity among all the NPs, it is meaningful that the activity of the mixture with Au NPs also resulted in a lower activity than the Au and the Au–Fe NPs. Note that the Au and the Fe_3O_4 particles were premixed and collected by centrifugation before the catalytic tests, to achieve the formation of an Au-Fe_3O_4 nanocomposite. Therefore, the catalysis experiments indicate the leading role of pure gold over all the other metals in the peroxidase mimic behaviour.

Discussion

In the oxidation reactions catalysed by peroxidases and their artificial mimics, hydrogen peroxide or organic hydroperoxides are reduced by interacting with a suitable substrate that acts as an electron donor.[4] The mechanism identified in natural peroxidases is the ping-pong process, also known as the double-shift reaction, in which the two redox substrates bind to the active site of the enzyme in successive steps of the catalytic cycle.[4,61] According to this mechanism, the product is generated and released before the second substrate binds to the enzyme. Theoretical and experimental studies have shown that NPs exhibit a similar mechanism, although it is not trivial to understand the exact steps due to the influence of multiple variables such as the size, morphology, composition, surface chemistry and reactivity of the NPs.[62–64] For instance, the enzymatic activity of transition metals with unpaired valence electrons such as iron, cobalt and copper is mainly driven by the change in the valence state due to hybridisation following the interaction between the metal and the substrate.[64–66] Conversely, for noble metals, the catalytic activity is due to the transfer of electrons to the substrate.[64–66] In both cases, two alternative mechanisms have been proposed for the peroxidase activity of metal nanomaterials, which are strictly dependent on the pH of the reaction environment.[64] In the first mechanism, the peroxidase activity is associated with the generation of •OH radicals after the adsorption of the H_2O_2 molecule, due to the breaking of the O–O bond. Two •OH radicals react to form a water molecule and an •O radical adsorbed on the nanoparticle surface, which can interact with the organic substrates by oxidising them and thus exerting the peroxidase-mimic activity. This is the case of nanozymes consisting of Fe_3O_4 NPs, where iron ions on the oxide surface can decompose H_2O_2 into •OH radicals, which in turn react with the redox substrate.[65]

The other mechanism explains the catalytic behaviour of artificial peroxidases based on the direct transfer of electrons from the nanoparticle to the substrate, without the intervention of any mediator.[64–66] This mechanism is based on the evidence that some types of nanozymes exhibit peroxidase activity that is not related to the generation of •OH radicals, as in the case of

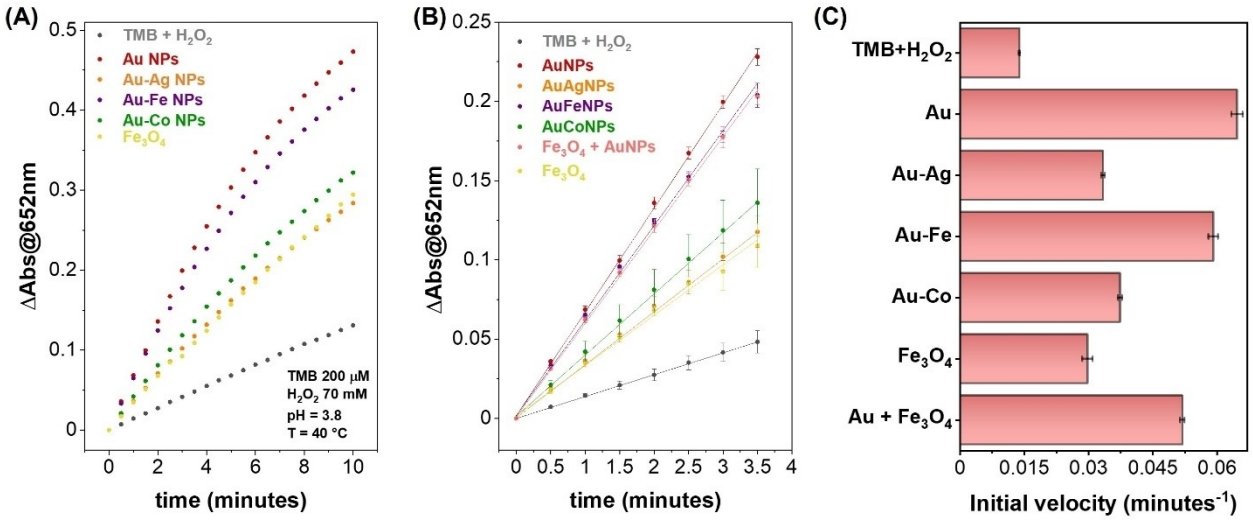

Figure 7. (A) Time evolution of the mean absorbance increase measured at 652 nm for the various samples tested in this study. (B) Magnification of (A) including the linear range considered for the linear regression which determined the initial velocities. Error bars are the semidispersion over two replicated experiments. (D) Plot of the initial velocity for all samples. Error bars are the semidispersion over two replicated experiments.

Co_3O_4 NPs.[66] Due to the high redox potential of the Co^{2+}/Co^{3+} pair, cobalt oxide nanoparticles are unable to efficiently generate •OH radicals. In this context, an electron transfer mechanism has been proposed in which the TMB substrate is directly oxidised by transferring the unshared electronic doublet of its amine groups to the cobalt oxide nanoparticle, on whose surface Co^{3+} is reduced to Co^{2+}. The redox catalytic cycle then closes with the transfer of the electron pair to the H_2O_2 and the restoration of the Co^{3+} species on the nanoparticle surface.

Concerning noble metal nanozymes, the first catalytic mechanism with free radical generation has been proposed for Pt nanoparticles functionalised on the surface with polyelectrolytes,[57] whereas the second mechanism with direct electronic transfer between TMB and H_2O_2 mediated by the metal nanoparticle has been proposed for a nanocomposite consisting of Au NPs and carbon dots.[60]

Since in this study the catalytic activity resulted higher with pure Au NPs than with all the Au nanoalloys, the mechanism proposed for gold NPs emerges as more efficient than those possible with nanostructures containing silver, iron or cobalt. Indeed, the TEM analysis showed that the Au NPs have the smallest average size among all samples, and it is widely recognized that a higher surface area/volume ratio favours the catalytic activity. In particular, the superior oxidation catalytic properties of smaller Au NPs have been related to the higher proportion of low coordination surface atoms, such as the "corners" and "edge atoms".[18]

Nonetheless, the average size alone does not correlate with the activity of the four samples, as shown in Figure 8A. In particular, the activity of Au and Au–Fe NPs is similar despite they have an average size of, respectively, 8 ± 4 nm and 18 ± 10 nm. On the other hand, the Au-Fe_3O_4 nanocomposite sample has lower activity than the Au–Fe nanoalloys, despite containing the pure Au NPs at the same mass of gold as in the reference Au NPs sample. This finding suggests that a crucial role is played by the available surface gold content in the different samples. In fact, the relative gold abundance at the topmost layer of the four samples, according to the XPS measurement, follows the activity trend Au > Au–Fe > Au–Co > Au–Ag, as shown in Figure 8B (black squares). Conversely, the catalytic activity is different for the three nanoalloys with comparable inner Au content (red circles in Figure 8B), indicating that the composition of the entire mass of NPs is not a reliable parameter for the interpretation of the observed peroxidase mimic behaviour.

Hence, the surface gold atoms constitute the dominant catalytically active sites for the TMB and H_2O_2 substrates, and the replacement of Au with the other metals in nanoalloys leads to a deterioration of the peroxidase mimic performance. Note that, although Au–Ag bimetallic nanostructures have been previously shown to exhibit stable peroxidase catalytic activity at acidic pH, which can be controlled by alloy composition and solution pH,[27] leaching of Ag at acidic pH and Au enrichment, as well as the role of surface capping agents, may explain the difference observed in that study concerning chemically synthesized NPs.

Concerning the catalytic activity evidenced by surface gold atoms over the other metals, it is worth noticing that, in general, catalysis depends on the ability of surface binding sites to alter the electronic structure of the reactants to activate specific bonds and produce intermediates that are ready to be transformed into more stable products.[10,12] The activation of chemical bonds does not occur in bulk gold due to the

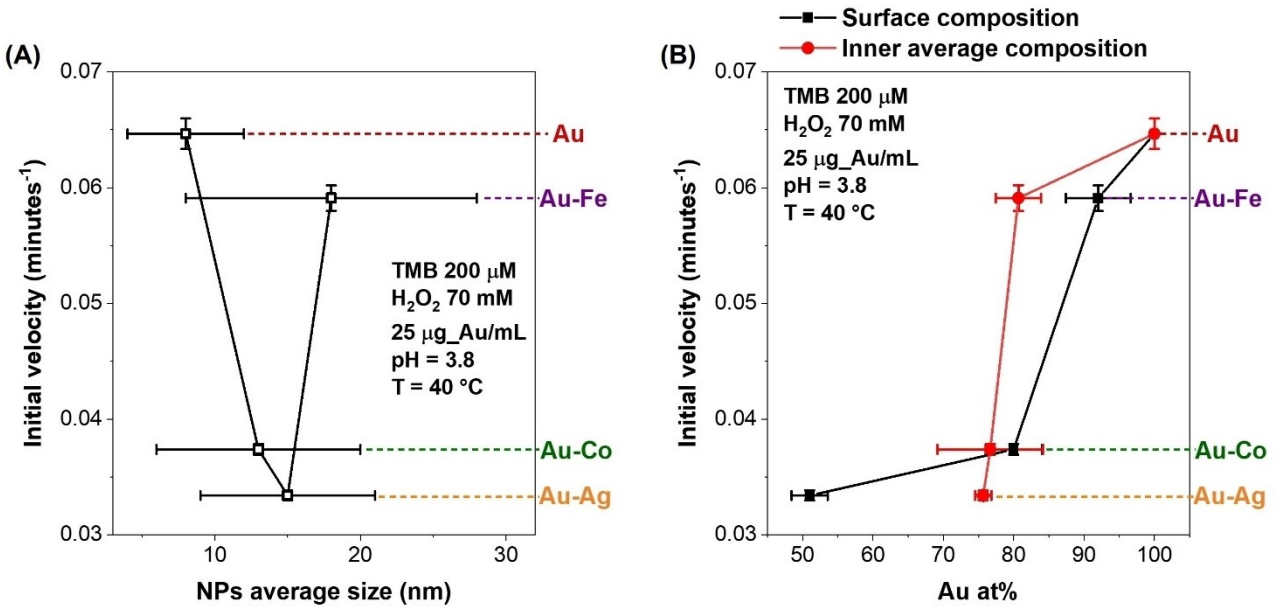

Figure 8. (A) Comparison of the initial velocity of the four samples versus the average NPs size. (B) Comparison of the initial velocity of the four samples versus the average atomic percentage of Au in the topmost surface layer of the NPs as measured by XPS before sputtering (black circles), or the inner atomic composition obtained from the various characterization techniques (red circles). Vertical error bars are the semidispersion over two replicated experiments. Horizontal error bars are the standard deviation over the average size (A) or composition (B).

relativistic effects leading to an unusually high hybridisation between the 6 *s* orbitals and the innermost 5*d* orbitals, which lowers the energy of the *d* electrons and makes the *s* electrons less available to participate in surface interactions, as they are more attracted to the atomic nucleus.[67] This is well described by the *d*-band model presented by Hammer and Nørskov,[68] which relates the noble behaviour of metals to two major properties, (1) the degree of filling of the anti-bonding states of adsorbed molecules and the *d*-band states of the metal, and (2) the degree of overlap between the electronic states of the adsorbate and the *d*-band states of the metal.[69] These two factors determine metal-adsorbate bond strength and the energy barrier required for adsorbate dissociation. Under typical conditions, gold exhibits both a filled metal-adsorbate-anti-bonded state and a high value of the metal-adsorbate coupling matrix element. The coexistence of these two properties makes bulk gold the noblest of all metals.[68] For example, the clean surface of Au(110)-(1×2) does not adsorb or dissociatively activate hydrogen or oxygen,[70] hence, this surface is completely inactive as a catalyst for hydrogen oxidation.

However, the binding or anti-binding character of the metal's *d*-band states depends on the bandwidth, which changes with the coordination number.[68,69] For example, for transition metals located to the right of the *d*-block (groups 8, 9, 10, and 11), the *d*-states move towards the Fermi level as the coordination number decreases.[69] When the *d*-band reaches higher energy than the Fermi level, the anti-bonding orbital remains empty for most molecule-surface interactions, leading to a strong bonding interaction between the two species.

It is well known that in nanoscale systems, such as metallic NPs, the surface atoms exhibit a high degree of undercoordination, causing them to participate in surface relaxation processes and organise themselves in configurations that are often very different from those of the bulk structure.[23] Due to the low coordination, metal NPs may therefore be able to bind adsorbates to their surface and activate them. According to this explanation, both the unoccupied and the *d*-band occupied electronic states of Au NPs increase in energy as the NPs size decreases.[71] This is referred to as nanoscaling effects on the reactivity of gold.[69] These size-dependent activities are thermodynamically explained in terms of changes in the adsorption free energies of the substrate and product.

Conclusions

Despite the catalytic properties of Au NPs have been extensively studied, there are ongoing efforts to improve their peroxidase mimic activity. In this respect, bimetallic NPs such as nanoalloys are considered promising candidates due to the unexpected behaviours and the synergistic effects which may result from the combination of the individual metals. Here Au–Ag, Au–Fe and Au–Co nanoalloys have been synthesized and their peroxidase mimic activity compared to pure Au NPs. Alloying did not result in improved catalytic activity compared to the Au NPs, which maintained the best catalytic response, yet comparable to that of the Au–Fe nanoalloys, while the Au–Co and Au–Ag nanoalloys performed worse. The results are correlated with the abundance of surface gold atoms in the different types of NPs, which thus represent the catalytically active sites for the oxidation process. On the other hand, it is shown that active oxidation nanocatalysts can be achieved with a lower content of gold by alloying it with iron, which is earth-abundant, non-toxic and low-cost. This can contribute to the development and understanding of peroxidase mimic nanocatalysts, which are of great relevance for a series of oxidation reactions exploited in biosensing, environmental monitoring and the development of greener chemical processes. Besides, nanoalloys of Au with sustainable elements deserve further investigation for the catalysis of other reactions typically relying on pure Au NPs, such as hydrogenation.

Acknowledgements

This research was funded by the University of Padova P-DiSC project "DYNAMO". JY acknowledges the China Scholarship Council for financial support (No. 202006880005). Open Access publishing facilitated by Università degli Studi di Padova, as part of the Wiley - CRUI-CARE agreement.

Conflict of Interests

The authors declare no conflict of interest.

Data Availability Statement

The data that support the findings of this study are available from the corresponding author upon reasonable request.

Keywords: nanoparticles · nanoalloys · peroxidase · nanozymes · gold · silver · iron · cobalt

[1] L. Que, W. B. Tolman, *Nature* **2008**, *455*, 333.
[2] X. Duan, S. C. Corgié, D. J. Aneshansley, P. Wang, L. P. Walker, E. P. Giannelis, *ChemPhysChem* **2014**, *15*, 974.
[3] J. Xie, X. Zhang, H. Wang, H. Zheng, Y. Huang, J. Xie, *TrAC Trends Anal. Chem.* **2012**, *39*, 114.
[4] R. Qu, L. Shen, Z. Chai, C. Jing, Y. Zhang, Y. An, L. Shi, *ACS Appl. Mater. Interfaces* **2014**, *6*, 19207.
[5] N. Lu, M. Zhang, L. Ding, J. Zheng, C. Zeng, Y. Wen, G. Liu, A. Aldalbahi, J. Shi, S. Song, et al., *Nanoscale* **2017**, *9*, 4508.
[6] Y. Liu, C. Wang, N. Cai, S. Long, F. Yu, *J. Mater. Sci.* **2014**, *49*, 7143.
[7] J. A. Nicell, H. Wright, *Enzyme Microb. Technol.* **1997**, *21*, 302.
[8] B. Valderrama, M. Ayala, R. Vazquez-Duhalt, *Chem. Biol.* **2002**, *9*, 555.
[9] M. Bortoli, M. Torsello, F. M. Bickelhaupt, L. Orian, *ChemPhysChem* **2017**, *18*, 2990.
[10] H. Wei, E. Wang, *Chem. Soc. Rev.* **2013**, *42*, 6060.
[11] F. Manea, F. B. Houillon, L. Pasquato, P. Scrimin, *Angew. Chemie Int. Ed.* **2004**, *43*, 6165.
[12] Y. Huang, J. Ren, X. Qu, *Chem. Rev.* **2019**, *119*, 4357.
[13] X. Xie, W. Xu, X. Liu, *Acc. Chem. Res.* **2012**, *45*, 1511.
[14] L. Gao, J. Zhuang, L. Nie, J. Zhang, Y. Zhang, N. Gu, T. Wang, J. Feng, D. Yang, S. Perrett, et al., *Nat. Nanotechnol.* **2007**, *2*, 577.
[15] Y. Jv, B. Li, R. Cao, *Chem. Commun.* **2010**, *46*, 8017.
[16] S. Wang, W. Chen, A. L. Liu, L. Hong, H. H. Deng, X. H. Lin, *ChemPhysChem* **2012**, *13*, 1199.

[17] Q. Liu, A. Zhang, R. Wang, Q. Zhang, D. Cui, *Nano-Micro Lett.* **2021**, *13*, 1.
[18] D. A. Panayotov, A. I. Frenkel, J. R. Morris, *ACS Energy Lett.* **2017**, *2*, 1223.
[19] S. Biswas, P. Tripathi, N. Kumar, S. Nara, *Sensors Actuators B Chem.* **2016**, *231*, 584.
[20] T. Ma, W. Yang, S. Liu, H. Zhang, F. Liang, *Catalysts* **2017**, *7*, 38.
[21] C. McVey, N. Logan, N. T. K. Thanh, C. Elliott, C. Cao, *Nano Res.* **2019**, *12*, 509.
[22] J. Zhang, J. Claverie, M. Chaker, D. Ma, *ChemPhysChem* **2017**, *18*, 986.
[23] H. Fang, J. Yang, M. Wen, Q. Wu, H. Fang, H. Yang, M. Wen, Q. S. Wu, *Adv. Mater.* **2018**, *30*, 1705698.
[24] V. Coviello, D. Forrer, V. Amendola, *ChemPhysChem* **2022**, *23*, e202200136.
[25] X. Meng, W. Zuo, P. Wu, Y. Song, G. J. Yang, S. Zhang, J. Yang, X. Zou, W. Wei, D. Zhang, et al., *Nano Lett.* **2024**, *24*, 51.
[26] J. L. Cann, A. De Luca, D. C. Dunand, D. Dye, D. B. Miracle, H. S. Oh, E. A. Olivetti, T. M. Pollock, W. J. Poole, R. Yang, et al., *Prog. Mater. Sci.* **2021**, *117*, 100722.
[27] W. He, X. Wu, J. Liu, X. Hu, K. Zhang, S. Hou, W. Zhou, S. Xie, *Chem. Mater.* **2010**, *22*, 2988.
[28] P. G. Kshirsagar, V. De Matteis, S. Pal, S. S. Sangaru, *Nanomaterials (Basel)* **2023**, *13*, 2471.
[29] J. Liu, X. Hu, S. Hou, T. Wen, W. Liu, X. Zhu, J. J. Yin, X. Wu, *Sensors Actuators B Chem.* **2012**, *166–167*, 708.
[30] K. Sytwu, M. Vadai, J. A. Dionne, *Adv. Phys. X* **2019**, *4*, 1619480.
[31] R. C. Forsythe, C. P. Cox, M. K. Wilsey, A. M. Müller, *Chem. Rev.* **2021**, *121*, 7568.
[32] I. Vassalini, L. Borgese, M. Mariz, S. Polizzi, G. Aquilanti, P. Ghigna, A. Sartorel, V. Amendola, I. Alessandri, *Angew. Chemie Int. Ed.* **2017**, *56*, 6589.
[33] D. T. L. Alexander, D. Forrer, E. Rossi, E. Lidorikis, S. Agnoli, G. D. Bernasconi, J. Butet, O. J. F. Martin, V. Amendola, *Nano Lett.* **2019**, *19*, 5754.
[34] S. X. Liang, L. C. Zhang, S. Reichenberger, S. Barcikowski, *Phys. Chem. Chem. Phys.* **2021**, *23*, 11121.
[35] E. D. Fakhrutdinova, A. V. Volokitina, S. A. Kulinich, D. A. Goncharova, T. S. Kharlamova, V. A. Svetlichnyi, *Materials (Basel).* **2024**, *17*, 527.
[36] C. Chowde Gowda, D. Chandravanshi, R. M. Tromer, A. Malya, K. Chattopadhyay, D. S. Galvão, C. S. Tiwary, *Appl. Phys. A Mater. Sci. Process.* **2024**, *130*, 1.
[37] V. Amendola, D. Amans, Y. Ishikawa, N. Koshizaki, S. Scirè, G. Compagnini, S. Reichenberger, S. Barcikowski, *Chem. - A Eur. J.* **2020**, *26*, 9206.
[38] D. Goncharova, M. Salaev, A. Volokitina, O. Magaev, V. Svetlichnyi, O. Vodyankina, *Mater. Today Chem.* **2023**, *33*, 101709.
[39] Y. Li, L. Xiao, Z. Zheng, J. Yan, L. Sun, Z. Huang, X. Li, *Nanomaterials (Basel)* **2023**, *13*, 2628.
[40] J. Theerthagiri, K. Karuppasamy, S. J. Lee, R. Shwetharani, H. S. Kim, S. K. K. Pasha, M. Ashokkumar, M. Y. Choi, *Light Sci. Appl.* **2022**, *11*, 1.
[41] S. Gu, J. Kaiser, G. Marzun, A. Ott, Y. Lu, M. Ballauff, A. Zaccone, S. Barcikowski, P. Wagener, *Catal. Letters* **2015**, *145*, 1105.
[42] D. Tiedemann, U. Taylor, C. Rehbock, J. Jakobi, S. Klein, W. A. Kues, S. Barcikowski, D. Rath, *Analyst* **2014**, *139*, 931.
[43] V. Coviello, D. Badocco, P. Pastore, M. Fracchia, P. Ghigna, A. Martucci, D. Forrer, V. Amendola, *Nat. Commun.* **2024**, *15*, 834.
[44] P. D. Josephy, T. Eling, R. P. Mason, *J. Biol. Chem.* **1982**, *257*, 3669.
[45] L. A. Marquez, H. B. Dunford, *Biochemistry* **1997**, *36*, 9349.
[46] V. Amendola, S. Scaramuzza, F. Carraro, E. Cattaruzza, *J. Colloid Interface Sci.* **2017**, *489*, 18.
[47] H. C. Chen, S. W. Chou, W. H. Tseng, I. W. P. Chen, C. C. Liu, C. Liu, C. L. Liu, C. H. Chen, C. I. Wu, P. T. Chou, *Adv. Funct. Mater.* **2012**, *22*, 3975.
[48] V. Amendola, M. Meneghetti, *Phys. Chem. Chem. Phys.* **2009**, *11*, 3805.
[49] A. Guadagnini, S. Agnoli, D. Badocco, P. Pastore, R. Pilot, R. Ravelle-Chapuis, M. B. F. Raap, V. Amendola, *ChemPhysChem* **2021**, *22*, 657.
[50] V. Amendola, M. Meneghetti, O. M. Bakr, P. Riello, S. Polizzi, S. Fiameni, H. Dalaver, P. Arosio, T. Orlando, C. de Julian Fernandez, et al., *Nanoscale* **2013**, *5*, 5611.
[51] D. A. Arena, R. A. Bartynski, S. L. Hulbert, *Many-Particle Spectrosc. Atoms, Mol. Clust. Surfaces*, Springer (Boston, MA, US), **2001**, 471.
[52] S. K. Parida, V. R. R. Medicherla, P. Bag, R. Rawat, T. Shripathi, N. Sahadev, D. Biswas, G. Adhikary, K. Maiti, *Adv. Sci. Lett.* **2014**, *20*, 792.
[53] A. M. Ferraria, A. P. Carapeto, A. M. Botelho Do Rego, *Vacuum* **2012**, *86*, 1988.
[54] A. P. Grosvenor, B. A. Kobe, M. C. Biesinger, N. S. McIntyre, *Surf. Interface Anal.* **2004**, *36*, 1564.
[55] M. C. Biesinger, B. P. Payne, A. P. Grosvenor, L. W. M. M. Lau, A. R. Gerson, R. S. C. Smart, *Appl. Surf. Sci.* **2011**, *257*, 2717.
[56] A. Guadagnini, S. Agnoli, D. Badocco, P. Pastore, D. Coral, M. B. Fernàndez van Raap, D. Forrer, V. Amendola, *J. Colloid Interface Sci.* **2021**, *585*, 267.
[57] S. Gu, S. Risse, Y. Lu, M. Ballauff, *ChemPhysChem* **2020**, *21*, 450.
[58] M. Drozd, M. Pietrzak, P. G. Parzuchowski, E. Malinowska, *Anal. Bioanal. Chem.* **2016**, *408*, 8505.
[59] X. Chen, X. Tian, B. Su, Z. Huang, X. Chen, M. Oyama, *Dalt. Trans.* **2014**, *43*, 7449.
[60] C. Zheng, W. Ke, T. Yin, X. An, *RSC Adv.* **2016**, *6*, 35280.
[61] S. Jin, C. Wu, Z. Ye, Y. Ying, *Sensors Actuators B Chem.* **2019**, *283*, 18.
[62] Y. Lin, J. Ren, X. Qu, *Adv. Mater.* **2014**, *26*, 4200.
[63] J. Lou-Franco, B. Das, C. Elliott, C. Cao, *Nano-Micro Lett.* **2020**, *13*, 1.
[64] B. Navyatha, S. Singh, S. Nara, *Biosens. Bioelectron.* **2021**, *175*, 112882.
[65] Z. Chen, J. J. Yin, Y. T. Zhou, Y. Zhang, L. Song, M. Song, S. Hu, N. Gu, *ACS Nano* **2012**, *6*, 4001.
[66] J. Dong, L. Song, J. J. Yin, W. He, Y. Wu, N. Gu, Y. Zhang, *ACS Appl. Mater. Interfaces* **2014**, *6*, 1959.
[67] T. Takei, T. Akita, I. Nakamura, T. Fujitani, M. Okumura, K. Okazaki, J. Huang, T. Ishida, M. Haruta, *Adv. Catal.* **2012**, *55*, 1.
[68] B. Hammer, J. K. Norskov, *Nature* **1995**, *376*, 238.
[69] J. K. Nørskov, F. Abild-Pedersen, F. Studt, T. Bligaard, *Proc. Natl. Acad. Sci.* **2011**, Vol. *108*, p. 937.
[70] A. G. Sault, R. J. Madix, C. T. Campbell, *Surf. Sci.* **1986**, *169*, 347.
[71] D. A. Panayotov, J. R. Morris, *Surf. Sci. Rep.* **2016**, *71*, 77.

Manuscript received: April 28, 2024
Revised manuscript received: July 17, 2024
Accepted manuscript online: July 18, 2024
Version of record online: September 16, 2024